

The signature of CDM substructure on gravitational lensing

M. Bradač^{1,2}, P. Schneider¹, M. Lombardi^{1,3}, M. Steinmetz^{4,5}, L.V.E. Koopmans⁶, and Julio F. Navarro⁷

¹ Institut für Astrophysik und Extraterrestrische Forschung, Auf dem Hügel 71, D-53121 Bonn, Germany

² Max-Planck-Institut für Radioastronomie, Auf dem Hügel 69, D-53121 Bonn, Germany

³ European Southern Observatory, Karl-Schwarzschild Str. 2, D-85748 Garching bei München, Germany

⁴ Astrophysikalisches Institut Potsdam, An der Sternwarte 16, D-14482 Potsdam, Germany

⁵ Steward Observatory, 933 North Cherry Avenue, Tucson, AZ 85721, USA

⁶ Space Telescope Science Institute, 3700 San Martin Drive, Baltimore, MD 21218, USA

⁷ Department of Physics and Astronomy, University of Victoria, BC V8P 1A1, Canada

Submitted to A&A, month ??,????

Abstract. We present a pilot study of the lens properties of quadruply imaged systems, lensed by N-body simulated galaxies. We investigate two different lens halos, one associated with an elliptical and one with a spiral galaxy. Flux-ratio anomalies observed in strong gravitational lensing potentially provide an indication for the presence of mass substructure in lens galaxies as predicted from CDM simulations. Using quadruply imaged systems generated by N-body simulated galaxies we particularly concentrate on the prediction that, for an ideal cusp caustic, the sum of the signed magnifications of the three highly magnified images should vanish when the source approaches the cusp. Strong violation of this cusp relation indicates the presence of substructure, regardless of the global, smooth mass model of the lens galaxy. We find that the level of substructure present in N-body simulations produces violations of the cusp relation comparable to those seen from observations. Higher-order catastrophes (e.g. swallowtails) can cause substantial changes in the cusp relation as predicted by a smooth model. Second, we confirm the dependence of flux anomaly distribution on the image parity and flux and find that the brightest minimum and saddle-point images are more affected by substructure than the fainter ones. In addition, there seems to be a trend that the brightest saddle point is demagnified w.r.t. the brightest minimum. Even though our results are fully numerical and properly include all mass scales, without making semi-analytic assumptions, they are ultimately limited by the mass resolution of single particles in the simulation determined by current computational limits.

Key words. cosmology: dark matter – galaxies: structure – gravitational lensing

1. Introduction

Whereas the current Cold Dark Matter (CDM) paradigm for structure formation is widely accepted, two major problems for CDM still remain. While simulations predict cuspy dark matter halos (Moore 1994), observed rotation curves of low surface brightness galaxies indicate that their dark matter halos have cores (Kravtsov et al. 1998; Swaters et al. 2000; van den Bosch & Swaters 2001; de Blok & Bosma 2002). The other is the apparent over-prediction of the small-scale power in CDM simulations. As was shown by Moore et al. (1999) and Klypin et al. (1999), the number of satellite halos seen in N-body simulations appears to far exceed the number of dwarf galaxies observed around the Milky Way. Particular discrepancies have been found for satellite masses $\lesssim 10^9 M_\odot$.

If one takes the observed satellites of the Milky Way as the total amount of substructure present, one needs to modify the CDM paradigm and include e.g. self-interacting dark matter (Spergel & Steinhardt 2000) or a cut-off in the power spectrum (which might occur in a warm dark matter-dominated universe, Bode et al. 2001; Colín et al. 2000). Another possibility pointed out by Stoehr et al. (2002) and Hayashi et al. (2003) is that the problem might be the misidentification of the observed satellites with the substructure seen in N-body simulations. Many mechanisms have been proposed which might prevent star formation in halos of mass $\lesssim 10^9 M_\odot$, making them too dim for observations (Bullock et al. 2000; Benson et al. 2002; Somerville 2002; Springel & Hernquist 2003). Zentner & Bullock (2003) investigate a semi-analytic model that describes the properties of galaxy-sized halo substructure. The effects of the “tilt” and overall normalisation of the primordial power spectrum are discussed. All these predictions need to be

tested within our own Galaxy as well as at cosmological distances.

Gravitational lensing is at present the only tool for investigating CDM substructure in galaxies outside the local group. As first noted by Mao & Schneider (1998), mass-substructure other than stars on scales less than the image separation can substantially affect the observed flux ratios in strong gravitational lens systems. Chiba (2002), Dalal & Kochanek (2002), Metcalf & Madau (2001), Metcalf & Zhao (2002), Keeton (2001), Mao & Schneider (1998) and Bradač et al. (2002) have argued that substructure can provide the explanation for the flux anomalies in various systems. Dalal & Kochanek (2002) further conclude that the amount of substructure needed to explain the flux ratios of quadruply-imaged systems broadly agrees with the CDM predictions. At least for some systems the flux mismatches are probably not just an artifact of oversimplified macromodels of the main lens galaxy (see e.g. Evans & Witt 2002; Metcalf & Zhao 2002). As discussed by Keeton (2003) and Chen et al. (2003), fluxes can be further affected by clumps of matter at a redshift different from that of the lens, lying along the line of sight between the observer and the source; however, this effect is not dominant.

Keeton (2001) and Gaudi & Petters (2002) recently focused on the magnification relations that should be satisfied by particular four-image geometries (so called “fold” and “cusp” configurations). Cusp and fold relations are model-independent predictions for the magnifications of highly magnified images (Blandford & Narayan 1986; Blandford 1990; Schneider & Weiss 1992; Mao 1992). Strictly speaking, however, they hold only for ideal “fold” or “cusp” configurations and it is therefore hard in some cases to disentangle the effects of the source being further away from the cusp from that of substructure, purely by employing these relations.

The influence of substructure can not only be seen on image flux ratios, but also in the structure of multiple-imaged jets. The lens system B1152+199 is a case of doubly-imaged jets, one of which appears bent, whereas the other is not (Metcalf 2002). Another explanation is that an intrinsic bend in the jet is simply magnified in one image, and produces only a small effect in the other.

Flux ratio anomalies can also be introduced by propagation effects in the interstellar medium (ISM) in the lens galaxy. Microlensing can change the flux ratios not only in the optical (e.g. Woźniak et al. 2000), but also at radio wavelengths (Koopmans & de Bruyn 2000). Flux ratios can further be affected by galactic scintillation and scatter broadening (Koopmans et al. 2003). Fortunately, these effects are frequency dependent and one can recognise them using multi-frequency observations.

These electromagnetic phenomena are similar for images of different parities. For substructure, however, Schechter & Wambsganss (2002) found that magnification perturbations should show a dependence on image parity. Microlensing simulations showed that the probability dis-

tributions for magnifications of individual images are no longer symmetric around the unperturbed magnification. The distribution can, depending on image parity, become highly skewed in the direction of demagnification. This skewness causes a substantial probability for the brightest saddle point image to be demagnified. The two saddle point images in the quadruply-imaged system are the ones with negative parity, the other two have positive parities and are called minima (they correspond to the local minima and saddle points in the arrival time surface). Observed lens systems seem to show this image parity dependence (Kochanek & Dalal 2003), and this indicates that the flux ratio anomalies arise from gravitational lensing, rather than propagation effects.

All these possible effects on flux ratios have placed some doubt as to whether the existence of substructure can be rigorously tested with strong lensing and on what the expected signal is. Several groups have been testing these predictions using a semi-analytic prescription for substructure (Metcalf & Madau 2001; Keeton et al. 2002; Dalal & Kochanek 2002; Kochanek & Dalal 2003).

In this paper, however, we use the direct output of different halos and projections of a galaxy obtained in N-body+gasdynamics as a lens galaxy. By using a semi-analytic prescription one overcomes the biggest problem we face, namely the problem of shot-noise in N-body simulations. Further, the problem of modelling becomes simpler, because one has an analytic model for the underlying macro-model. However, by using the direct output of an N-body simulated galaxy, one does not make any assumption about the mass profiles of the macro model, or the substructure. Down to the resolution scales of the simulation we therefore believe we have a better comparison with a realistic galaxy.

This paper is structured as follows. In Sect. 2 we first give the main properties of the N-body simulations we use. We also introduce an improved smoothing scheme compared to Bradač et al. (2002) and give a description of how to extract lensing properties from N-body simulations. In Sect. 3 we focus on the cusp relation for simulated lens systems. Sect. 4 describes the modelling of synthetic images and the phenomenon of suppressed saddle points. We conclude and give an outlook in Sect. 5.

2. Strong lensing by a simulated galaxy

N-body simulations can provide a powerful benchmark for testing the effects of substructure on strong lensing. One can simulate ideal conditions in which propagation effects of the ISM can be ignored and search for the signature of substructure. The drawback of this method at present lies in the resolution available for simulations that include dark matter, gas and star particles. This limits our analysis to mass clumps of masses $\gtrsim 10^7 M_\odot$. However, since the mass resolution is advancing rapidly, this will soon no longer be a problem. The results here should therefore be regarded as a pilot study at the limits of current simulation techniques.

As in Bradač et al. (2002), we used the cosmological N-body simulation data for several realisations of galaxies including gas-dynamics and star formation (Steinmetz & Navarro 2003). This time we investigate two different halos, each of them in three different projections. The simulations were performed using GRAPESPH, a code that combines the hardware N-body integrator GRAPE with the Smooth Particle Hydrodynamics technique (Steinmetz 1996).

In Table 1 the properties of the halos are listed. In both cases the original simulated field contains approximately 300 000 particles. The simulation is contained within a sphere of diameter 32 Mpc which is split into a high-resolution sphere of diameter 2.5 Mpc centred around the galaxy and an outer low-resolution shell. Gasdynamics and star formation are restricted to the high-resolution sphere, while the dark matter particles of the low-resolution sphere sample the large scale matter distribution in order to appropriately reproduce the large scale tidal fields (see Navarro & Steinmetz 1997 and Steinmetz & Navarro 2000 for details on this simulation technique). From the original simulated field we take a cut-out cube of size $\sim 200^3$ kpc 3 centred on a single galaxy. This area lies well within the high-resolution sphere and is void of any massive intruder particles from the low-resolution shell.

All simulations were performed in a Λ CDM cosmology ($\Omega_0 = 0.3$, $\Omega_\Lambda = 0.7$, $\Omega_b = 0.019/h^2$, $\sigma_8 = 0.9$). They have a mass resolution of $1.26 \times 10^7 M_\odot$ and a spatial resolution of 0.5 kpc. A realistic resolution scale for an identified substructure is typically assumed to be ~ 40 particles which corresponds to $5 \times 10^8 M_\odot$. The quoted mass resolution holds for gas/stars. The high-resolution dark matter particles are about a factor of 7 ($= \Omega_0/\Omega_b$) more massive. A detailed analysis of the photometric and dynamical properties of the simulated halos we used here was carried out in Meza et al. (2003) for the elliptical and Abadi et al. (2002a,b) for the disc galaxy.

Table 1. Properties of the two simulated halos we used. z_1 denotes the redshift of the halo, z_s is the redshift of the source. N_{bar} , N_{DM} , and N_{str} are the numbers of baryonic, dark matter particles and “stars” respectively, present in the cut-out of the simulation we used (note that even within one family particles have different masses). M_{tot} is the total mass of the particles we used.

Halo	Elliptical	Spiral
z_1	0.81	0.33
z_s	3.0	3.0
N_{bar}	12 000	20 000
N_{DM}	17 000	26 000
N_{str}	70 000	110 000
M_{tot}	$1.5 \cdot 10^{12} M_\odot$	$0.5 \cdot 10^{12} M_\odot$

2.1. Delaunay triangulation smoothing technique

From the particle distribution irregularly sampled in the simulation box, we reconstruct the density field. We apply a smoothing procedure and then project the resulting particle distribution to obtain the surface mass density κ map. In Bradač et al. (2002) it was shown that a more sophisticated smoothing method should be employed for the data analysis than smoothing with a Gaussian kernel. A method is needed that adapts the kernel size in order to increase the signal to noise of the reconstructed field. For this purpose, we make use of the Delaunay tessellation technique from Schaap & van de Weygaert (2000).

We perform a three-dimensional Delaunay triangulation using the QHULL algorithm (Barber et al. 1996). The density estimator from Schaap & van de Weygaert (2000) is evaluated at each vertex, and in order to obtain the κ -map we interpolate values of the density at each three-dimensional grid point. Finally, we project the resulting values onto a two-dimensional grid.

Since the N-body simulations contain three independent classes of particles (gas, stars, and dark matter particles, each having different masses), we perform the procedure described above for each group separately and obtain the final κ map by adding up the contributions from all three classes.

The Delaunay tessellation method performs very well in comparison to the standard Gaussian smoothing technique used in Bradač et al. (2002), or an adaptive Gaussian smoothing technique (see also Schaap & van de Weygaert 2000). Since it is parameter free, it adjusts the scale of the smoothing kernel itself such that the regions of low noise (i.e. where the particle density is highest) are effectively smoothed less than regions with high noise. Also the shape of the kernel is self-adaptive. Hence, this method is very useful for the analysis of galaxies with high dynamic range and significant structure in the mass distribution (e.g. mass clumps and spiral arms).

2.2. Estimating the noise properties

A drawback of using the Delaunay tessellation method is that the noise evaluation for the final surface mass density map is non-trivial. For example, with a Gaussian kernel one can get an estimate for the noise by simply looking at the number of particles in a smoothing area (for a more detailed estimate, see Lombardi & Schneider 2002). When using the tessellation technique, such an approach is not viable.

One possible approach for estimating the error is to use the bootstrapping technique (see e.g. Heyl et al. 1994). Ordinarily we calculate physical properties (e.g. κ -map) by using all n particles from the simulation. In order to create a bootstrap image one has to randomly select n particles out of this simulation with replacement; i.e. some of the particles from the original simulation would be included more than once, some not at all. In other words, we

randomly generate n numbers from 1 to n and they represent the bootstrapped set of particles. E.g. if a particle is included x times in a bootstrapped map, we put a particle at the same position with x times its original mass. After creating an ensemble of such images and calculating the desired physical quantity for each of them, one can then make an error estimation.

A problematic issue in our case is the creation of an ensemble of κ -maps from the bootstrapped images. Whereas the tessellation itself is done very quickly, the interpolation of density on a grid is a process that takes a few CPU days on a regular PC. We therefore limit ourselves to 10 bootstrapped maps, as described above, and compare them with the original maps. We perform this analysis for the elliptical halo only, because it's computational expensive and we don't expect systematic differences.

For each pixel i we calculate the associated error using

$$\sigma^2(\kappa_i) = \frac{1}{M-1} \sum_{m=1}^M (\kappa_i^m - \langle \kappa_i \rangle)^2 \quad (1)$$

where $\langle \kappa_i \rangle$ is the average value of κ at pixel i averaged over all $m = M$ bootstrapped maps; in our case $M = 10$.

This procedure gives us an estimate for the error on κ . Within the critical curves, i.e. $\kappa \gtrsim 0.5$ the average noise $\sigma(\kappa_i)/\langle \kappa \rangle$ is of the order of $\lesssim 5\%$.

2.3. Strong lensing properties

Having obtained the κ -map, we then calculate the lens properties on the grid (2048×2048 pixels). The Poisson equation for the lens potential ψ

$$\nabla^2 \psi(\boldsymbol{\theta}) = 2 \kappa(\boldsymbol{\theta}) \quad (2)$$

is solved (on the grid) in Fourier space by the DFT (Discrete Fourier Transformation) method. For this purpose, we used the publicly available C library FFTW ("Fastest Fourier Transform in the West") written by Frigo & Johnson (1998). In order to reduce the boundary effect, padding was introduced. More precisely, the DFT was performed on a 4096×4096 grid, where one fourth of the grid contains the original κ map and the rest is set to zero.

From this point one can proceed in two ways. One can calculate the two components of the shear $\gamma_{1,2}$ and the deflection angle $\boldsymbol{\alpha}$ by multiplying the potential in Fourier space by an appropriate kernel. Since we calculate the Fourier transform of the potential on a finite grid, we effectively filter out high spatial frequency modes. By multiplying the transform with different kernels for $\gamma_{1,2}$ and $\boldsymbol{\alpha}$, these final maps do not necessarily correspond to the same κ map. The effect is very small, but it shows up as we approach the critical curves. Therefore, it is better to only calculate the lens potential ψ using DFT and obtain the lens properties by finite differencing. The latter method is also less CPU-time and memory consuming.

The simulated galaxy is a field galaxy. However, most of the lenses in quadruple image systems are members

of groups. To make our simulated galaxies as closely related to realistic systems as possible, we add external shear to the Jacobi matrix (evaluated at each grid point). The shear components were the same for each projection and all halos, and chosen to be

$$\gamma_1^{\text{ext}} = -0.04, \quad \gamma_2^{\text{ext}} = -0.16;$$

they correspond to the shear of the best-fit singular-isothermal ellipse model with external shear for the lens B1422+231 in Bradač et al. (2002). Figure 1 show the magnification maps of the elliptical and edge-on spiral galaxy. The corresponding caustic curves (for a source at $z = 3$) were obtained by projecting the points of high magnification from the image plane to the source plane using deflection angle information. They are plotted in white(red) in Fig. 2a for the elliptical and Fig. 4c for the edge-on spiral galaxy.

2.4. Four-image systems of N -body simulated galaxies

Finally we generate different four-image systems using individual simulated galaxies. For each halo and projection direction, regions in the source plane where five images form were determined. The image plane is projected back to the source plane using the magnification and deflection angle maps. We used the grid search method from Blandford & Kochanek (1987) to find the pixels enclosed by the asteroid caustic and approximate image positions. Then the MNEWT routine from Press et al. (1992) is applied and the lens equation is solved for the image positions. For this step, we interpolate the deflection angle between the grid points. We use bilinear interpolation and bicubic spline, and both methods give comparable results. Once we have the image positions, the magnification factors are calculated and the four brightest images are chosen. These represent the "observable" images; the fifth image is usually too faint (except in the regions where more than five images are formed) and therefore likely to escape observation.

3. The cusp relation

Having obtained synthetic four-image systems we can investigate their basic properties. There are three basic configurations for four-image systems: fold, cusp, and cross. They correspond to a source located inside the asteroid caustic, close to a fold, a cusp or near the centre, respectively (see e.g. Keeton 2001). All configurations have been observed, and even though one would naively think that fold and cusp images are rare among observed lenses, they are in fact frequently observed due to the large magnification bias. In this section we will mainly concentrate on cusp image configurations.

² For distance calculations throughout the paper we assume an Einstein-de-Sitter Universe and the Hubble constant $H_0 = 65 \text{ km s}^{-1} \text{ Mpc}^{-1}$.

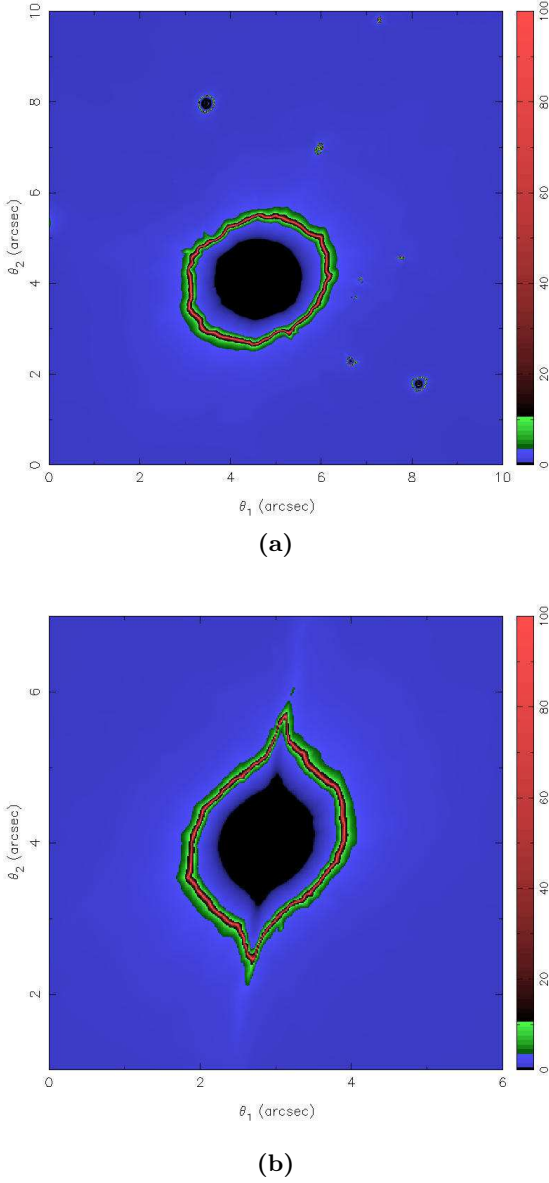


Fig. 1. The magnification map of the simulated elliptical (a) and edge-on spiral (b) galaxy. External shear is added in the evaluation of the magnification map to account for neighbouring galaxies (see text). Lighter (red) regions represent high magnifications. The units on the axes are arcseconds, one arcsecond in the *lens* plane corresponds to approximately 7 kpc in (a) and 5 kpc in (b).²

The behaviour of gravitational lens mapping near a cusp was first studied by Blandford & Narayan (1986), Blandford (1990), Schneider & Weiss (1992), and Mao (1992), who investigated the magnification properties of the cusp images and concluded that the sum of the signed magnification factors of three merging images approaches

zero as the source moves towards the cusp. In other words (Keeton 2001),

$$R_{\text{cusp}} = \frac{\mu_A + \mu_B + \mu_C}{|\mu_A| + |\mu_B| + |\mu_C|} \rightarrow 0, \text{ for } \mu_{\text{tot}} \rightarrow \infty, \quad (3)$$

where μ_{tot} is the unsigned sum of magnifications of all four images, and A, B and C is the triplet of images forming the smallest opening angle. By the opening angle, we mean the angle measured from the galaxy centre and being spanned by two images of equal parity. The third image lies inside such an angle.

3.1. The cusp relation in an *N*-body simulated elliptical galaxy

The cusp relation (3) is an asymptotic relation and holds when the source approaches the cusp from inside the asteroid. One can derive the properties of lens mapping close to critical curves using a Taylor expansion of the Fermat potential around a critical point (see e.g. Schneider & Weiss 1992). Such calculations are very cumbersome and therefore it is difficult (if not impossible) to explore the influence of arbitrary substructure analytically. In practice, we can calculate R_{cusp} for the *N*-body simulated systems. Smoothing the original κ -map on different scales then gives an indication of the influence of substructure on R_{cusp} .

The three cusp images [designated as A, B and C in (3)] are chosen according to the image geometry. Since we know the lens position, this procedure is straightforward and foolproof. We have identified the triplet of images belonging to the smallest opening angle (described above). Since we know the image parities and magnifications, one is tempted to identify the three brightest images as the cusp images (e.g. as in Quadri et al. 2002). However, due to the presence of shear and substructure this can easily lead to misidentifications.

Figure 2a shows the caustic curve in the source plane for the simulated elliptical at a redshift of $z_1 = 0.81$. The source is at a redshift of $z_s = 3$. Approximately 30 000 lens systems are generated with source positions inside the asteroid caustic. R_{cusp} is plotted in colour. The apparent discontinuities originate from different image identification. In the very centre of the caustic the meaning of “cusp image” is ill defined. As the source moves in the direction of the minor or major axes we chose different subsets of three cusp images and therefore the discontinuity arises.

The remaining panels of Fig. 2 show the effect of smoothing the surface mass density κ map with Gaussian kernels characterised by standard deviation σ_G . The values for σ_G were chosen to be $\sigma_G \sim 1, 2, 5$ kpc for panels (b), (c) and (d) respectively. Note that we do not smooth the κ -map directly. First we obtain the smooth model κ_{smooth} for the κ -map by fitting elliptical contours to the original map using *IRAF*.*STSDAS* package *ellipse*. We subtract κ_{smooth} from κ and smooth the difference using different Gaussian kernels. We then add the resulting

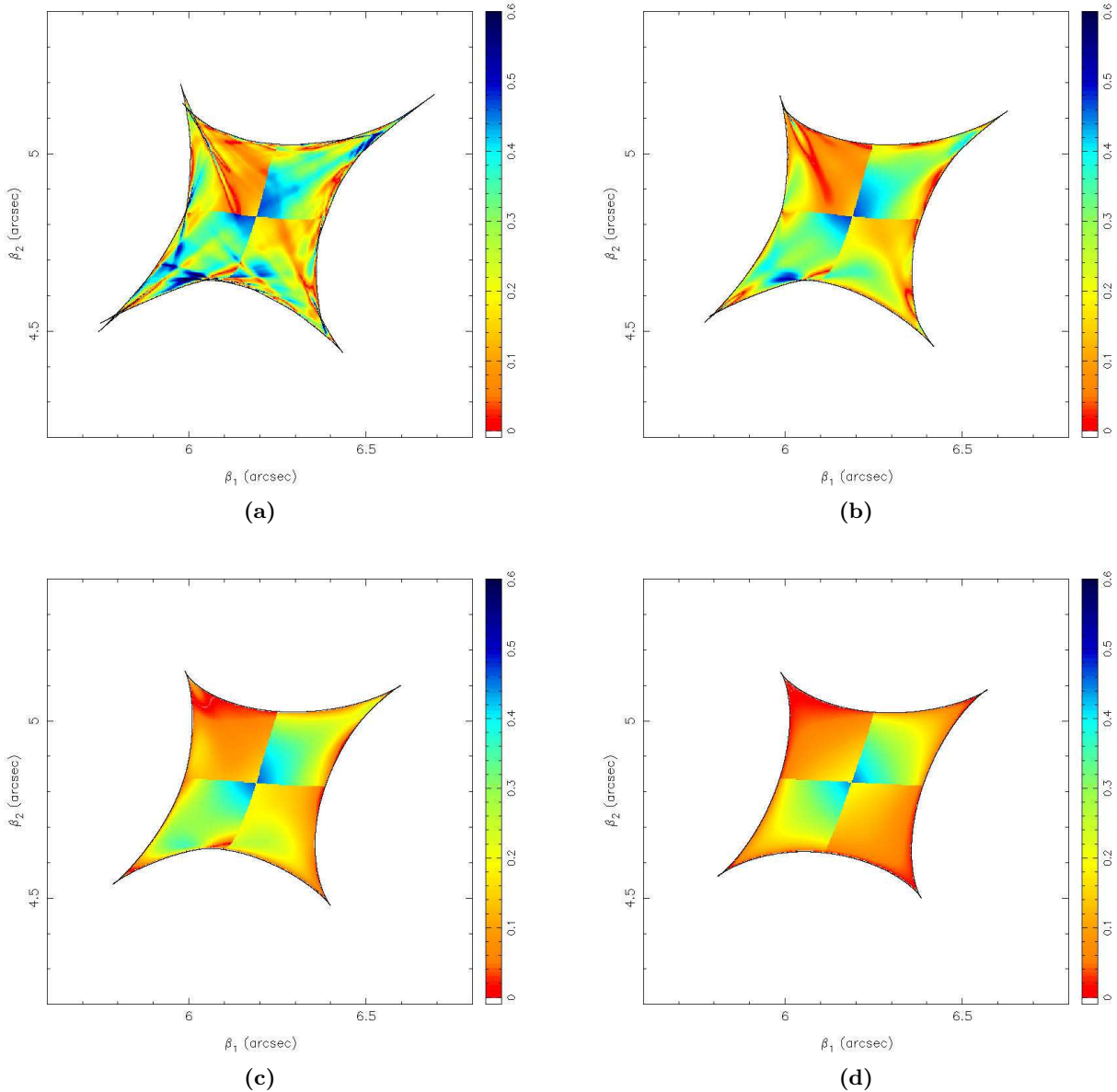


Fig. 2. The cusp relation R_{cusp} for the N-body simulated elliptical galaxy at a redshift of $z_l = 0.81$. The source was put at a redshift of $z_s = 3$ and approx. 30 000 systems were generated that lie inside the asteroid caustic. R_{cusp} is plotted in colour, for sources close to the cusp the smooth models would predict $R_{\text{cusp}} \sim 0$ (i.e. red colour). The deviations are due to the substructure. Due to magnification bias most of the observed lenses correspond to the fold and cusp configurations. Discontinuities in the maps arise when the source moves in the direction of the minor or major axes, since we chose different subsets of three cusp images. On top we plot the caustic curve. Panel (a) shows R_{cusp} for the original image, whereas panels (b)–(d) show the cusp relation for the models where we additionally smoothed the substructure (see text) with a Gaussian kernel characterised by standard deviation $\sigma_G \sim 1$ kpc (b), $\sigma_G \sim 2$ kpc (c) and $\sigma_G \sim 5$ kpc (d).

map back to the κ_{smooth} . In this way the overall radial profile of the mass distribution is not affected.

The effect of smoothing on the cusp relation is clearly visible. From Fig. 2d one sees that the substructure is washed out when smoothing on scales of $\sigma_G \sim 5$ kpc is applied. As we go to smaller smoothing lengths, the effects of substructure become clearly visible. In the extensions of swallowtails there is a region where the cusp relation

is strongly broken; however further out, a swallowtail can cause the cusp relation to change the trend and go to zero (due to high-magnification systems being formed in such region).

Finally, the cusp relation behaves differently when the source moves along the major or along the minor axis (see especially Fig. 2d). This is a generic feature for smooth elliptical models and can easily be calculated for e.g. an el-

liptical isopotential model (see e.g. Schneider et al. 1992). We use this model since it is analytically tractable for source positions along the major and minor axis. In Fig. 3 we plot the cusp relation for the source moving along the major(minor) axis as a thick(thin) solid line for the elliptical isopotential model with $\epsilon = 0.15$. As the source approaches the cusp, $R_{\text{cusp}} \rightarrow 0$ for both source positions, however the slope is different. We also plot the total magnification factor of the three cusp images, i.e. $\mu_{A+B+C} = |\mu_A| + |\mu_B| + |\mu_C|$ as a thick(thin) dashed line.

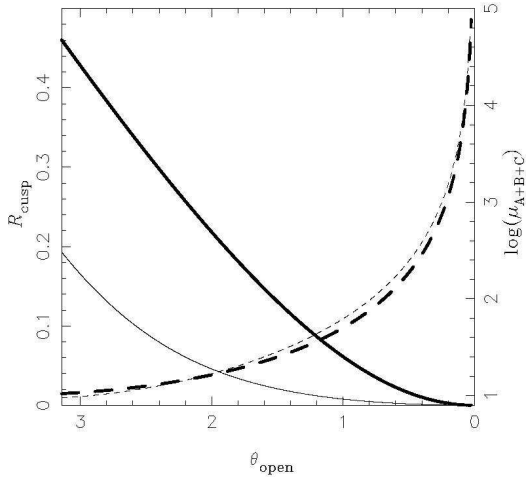


Fig. 3. R_{cusp} for a simple elliptical isopotential lens model with $\epsilon = 0.15$. R_{cusp} is plotted as a thick (thin) solid line for sources along the major (minor) axis. θ_{open} represents the angle measured from the position of the galaxy, spanned by two “outer” cusp images (A and C). The opening angle π means that the source is located at the centre (images A, C and the galaxy lie on the same line). When the source approaches the cusp, $\theta_{\text{open}} \rightarrow 0$. The total magnification for the three cusp images μ_{A+B+C} is plotted as a thick (thin) dashed line for sources along the major (minor) axis.

3.2. The cusp relation in an N-body simulated spiral galaxy

The procedure described above was applied to three different projections of the elliptical halo and very similar conclusions could be made. The question is, however, how much those conclusions depend on the specific morphological type of the galaxy itself. In order to investigate this we also followed a procedure similar to the above for a simulated spiral galaxy.

In this case, however, we did not look at the effects of additional smoothing. It is difficult to subtract the smooth model, as the galaxy consists of a bulge, warped disk and extended halo. It can not simply be fitted by ellipses. If we were to smooth the edge-on projection with a Gaussian

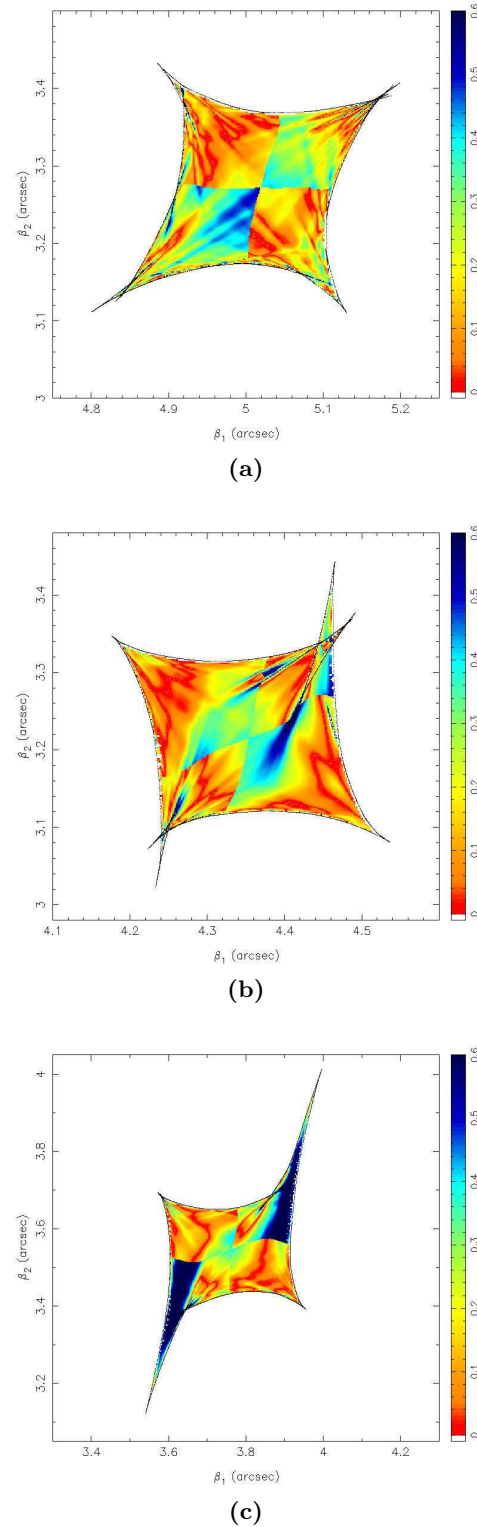


Fig. 4. The cusp relation for the N-body simulated spiral galaxy at a redshift of $z_l = 0.33$. The source was put at a redshift of $z_s = 3$ and approx. 10 000 systems were generated which lie inside the asteroid caustic. R_{cusp} is plotted in colour. On top we plot the caustic curve. Panels (a), (b), and (c) show three different orthogonal projections of the halo, (a) corresponds to the face-on, (b) and (c) to the edge-on projection. Panel(c) corresponds to the magnification map in Fig. 1b.

kernel, we would also wash out the (in our case warped) disc. We include the analysis of the cusp relation for this halo in order to show the effect of the disc on R_{cusp} .

Figure 4 shows the cusp relation of an N-body simulated spiral galaxy, this time shown in three projections. The disc clearly plays a role for the edge-on projection (see Fig. 4b,c), whereas the face-on projection is similar to the elliptical halo. Especially in Fig. 4c, where the disc extent in projection is smaller than the typical image separation, the cusp relation in the upper-right and lower-left cusp is highly violated. This direction corresponds to the orientation of the disc.

3.3. Observed cusp relation

In this section we compare predictions of R_{cusp} from N-body simulated galaxies with the values from observed lens system. Unfortunately the number of observed systems is not high; seventeen four-image systems have been published (see Keeton et al. 2002 for a summary), and four of them are believed to show a typical cusp geometry (see Table 2).

Note that relation (3) is model independent and can only be broken in the presence of substructure on scales smaller than the image separation. Hence, if the smooth model provided an adequate description of the lens galaxy, one would expect $R_{\text{cusp}} \sim 0$ for these lenses. This is clearly not the case and for this reason it is impossible to explain their flux ratios using simple, smooth models.

If we make a comparison with simulations, one can see that the pattern in Fig. 2d clearly does not explain the observed R_{cusp} of these four lenses. On the other hand, substructure on kpc scales and below provides enough perturbations to R_{cusp} to explain the observed values.

The question arises, however, whether we can conclude that we indeed see the effects of substructure from the value of R_{cusp} alone. Keeton et al. (2002) argued that the cusp relation alone does not reveal anomalous flux ratios in B1422+231. Still, detailed modelling for this system shows that the flux ratios are indeed anomalous. On the other hand, the simulated spiral galaxy shows violation of R_{cusp} even though there are no clear mass clumps present in the region where images are formed. Therefore

Table 2. The values for R_{cusp} taken from Keeton et al. (2002) for four lens systems showing a typical cusp geometry.

Lens	R_{cusp}
B2045+265	0.52 ± 0.04
B0712+472	0.26 ± 0.06
RX J0911+0551	0.22 ± 0.06
B1422+231	0.18 ± 0.06

one has to be cautious when making conclusions about substructure based on the value of R_{cusp} only.

3.4. The influence of noise on the cusp relation

In principle, the simulated cusp-relation can be reliably compared with observations only if we know the noise properties of our simulation. On the other hand, we know that physical substructures on scales $\sim 10^6 M_{\odot}$ can substantially affect the flux ratios for highly magnified images (see e.g. Mao & Schneider 1998). These two effects need to be disentangled and therefore an analysis of the noise is needed.

From the bootstrapping procedure described in Sect. 2.2 we also get an estimate of the error in the cusp relation. We estimated the noise of R_{cusp} using a similar technique we used for κ in (1). Here, however, we do not make the analysis directly in the source plane by subtracting the maps pixel-by-pixel. The problem is that bootstrapping slightly changes the shape of the caustic curve (see also Fig. 6). Since we never observe the source plane directly, we can not distinguish between two shifted, identical caustics in reality. We therefore have to match different bootstrap maps in the image plane. We compare the image positions generated by each source in the original frame with those generated by bootstrapped lenses. Thus for each source position in the original map (see Fig. 2a), we search for the source position in the bootstrapped map such that the four image positions from both maps differ as few as possible.

In principle, one can also perform the ray-tracing again and calculate image fluxes for the position in the original map by using the bootstrapped-lens properties. However this is not necessary, since our grid in the source plane is fine enough and we only need the approximate error estimate. Figure 5 shows the estimated absolute error of $\sigma(R_{\text{cusp},i})$ for the elliptical halo from Fig. 2a. As described above, each value of $\sigma(R_{\text{cusp},i})$, plotted in colour, does not correspond to the error for a source position, but refers to the error of the system with image positions similar to the original ones.

The absolute error is of the order of 0.1 and gets slightly larger at the regions of the swallow tails. This is, however, not the effect of substructure vanishing in individual bootstrapped realisations. It is rather the effect of slight position changes of individual clumps. If one looks at the individual caustic curves of bootstrapped halos (see Fig. 6) the swallow-tails are present in all realisations, although they change their positions slightly. Since this hardly affects the image positions we cannot perfectly match the source positions i' with the original source position i in these regions; thus we are overestimating the true error.

4. Lens models for synthetic image systems

We have tried to fit the synthetic systems using a singular isothermal ellipse model with external shear (SIE+SH)

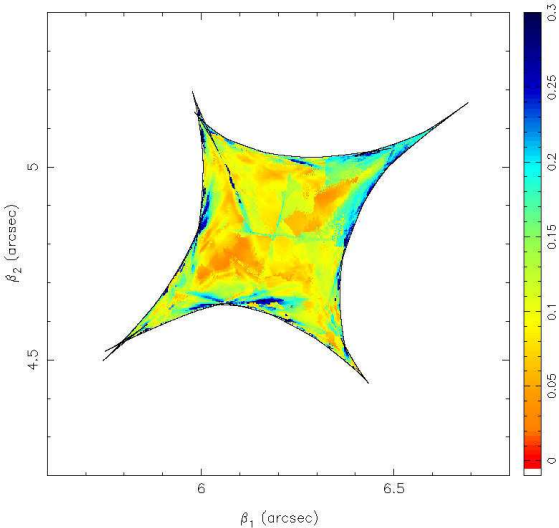


Fig. 5. The estimated absolute uncertainty $\sigma(R_{\text{cusp},i})$ of the cusp relation, calculated using the bootstrap analysis described in Sect. 2.2. Note that the colour coding has changed as compared with the other figures in this paper. The errors plotted for each source position were calculated using the systems from bootstrapped maps having similar image positions as the system generated by the original lens; i.e. from Fig. 2a (see text).

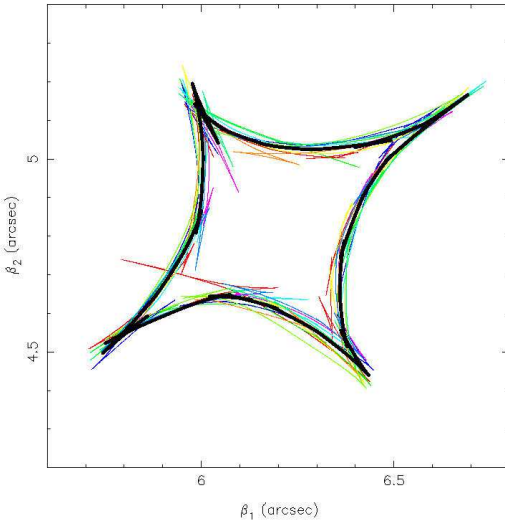


Fig. 6. The original caustic curve (thick line) of the halo from Fig. 2a and the corresponding caustic curves from the ten bootstrapped maps plotted on top (thin lines).

(Kormann et al. 1994). We have not included the flux ratios in the fit, as they are affected by the substructure. Furthermore, we kept the lens position fixed. Using only image positions we thus have 7 parameters and 8 constraints (as parameters we used lens strength, two components of the ellipticity of the lens, two external shear

components and the source position, and we have 4 image positions as constraints).

4.1. Surface mass density profile

We find that the average unsigned magnification factors predicted by the SIE+SH model are higher than those taken from N-body simulations. This is true for all systems generated with the same halo and is a consequence of the mass profile being steeper than isothermal at the typical position where the images are formed.

We have calculated the surface mass density κ profile for the N-body simulated elliptical by fitting the iso- κ elliptical contours to the original κ map using the **IRAF**.**STSDAS** package **ellipse**. For $\theta \lesssim 0.1$ arcsec the profile is very close to isothermal with slope -1.0 ± 0.2 . At $\theta \gtrsim 0.1$ arcsec the profile becomes steeper than isothermal with slope -1.9 ± 0.2 . The break radius, where the profile becomes steeper than isothermal, is much smaller than the radius where images are formed.

We therefore constantly over-predict the magnifications using an isothermal profile. In order to deal with this problem, one would have to use a power-law profile with the index mentioned above for the lens modelling, instead of SIE. However, fitting such a profile requires much more CPU time than fitting an SIE profile; in order to get the magnification matrix and the deflection angle one has to deal with either evaluations of hypergeometric functions or numerical integrations (Grogan & Narayan 1996; Barkana 1998). Such modelling is therefore more time consuming and as such not practical for applying to a few 10 000 sources. Moreover, we are not searching for the best fit macro-model, but rather pretending that we observe the systems and try to fit them with the standard model used for observed lenses. Since we only observe the flux ratios and not the magnification factors, it is impossible to compare magnification factors in practice. Thus one cannot spot the difference in profiles using only this consideration when dealing with real lens systems.

4.2. Suppressed saddle points

It was first noted by Witt et al. (1995) that the expected flux fluctuations due to microlensing differ for saddle points as opposed to minima in the case of stellar mass perturbers. This was further investigated by Schechter & Wambsganss (2002) who conclude that a stellar mass component added to a smoothly distributed mass can cause a substantial probability for the saddle point image in the fold configuration to be demagnified w.r.t. the minimum.

Recently, Kochanek & Dalal (2003) and Keeton (2003) investigated the effect of singular isothermal sphere (SIS) mass clumps on the flux perturbations for images of different types. Their conclusions were similar; SIS perturbers also cause the brightest saddle point image to behave statistically differently as compared to the minimum.

The answer to whether the flux anomalies depend upon the image parity for observed lenses would mean a big step forward in identifying flux anomalies either with substructure or with propagation effects. Namely, if the observed flux anomalies depend upon the image parity and its magnification we can set limits on the influence of the ISM (see Kochanek & Dalal 2003).

Modelling our synthetic images with the SIE+SH model (as described above) we have plotted the cumulative distribution of flux residuals in Fig 7. We took the systems generated by the elliptical halo (see also Fig. 2a) and included only the ones with “observed” total unsigned magnification $\mu_{\text{tot}} > 20$ in the calculations. This choice was made to pick out the systems which have highly magnified images and therefore are most likely to be affected by substructure. We repeated the whole procedure with the same halo, but smoothed on a scale of $\sigma_G \sim 5$ kpc. In Fig. 7 we plot the cumulative distribution of flux residuals only for the original model; for the smooth model (not shown) we essentially do not see any difference among images of different parity.

The first thing to notice is that the cumulative distribution is much broader for the brighter minimum and saddle point. This is in accordance with the conclusions from Mao & Schneider (1998); the higher the magnification, the more is the image flux affected by substructure. Among the two magnified images there is a trend that the saddle point is demagnified compared to the brighter minimum. We have investigated two other orthogonal projections of the mass density of the same halo and we find that qualitatively the results do not change with projection.

The effect, however, is not as pronounced as in Kochanek & Dalal (2003). The reason is two-fold. First, our simulations have a resolution of $\sim 10^7 M_\odot$ and structure at this scale and below is suppressed when using Delaunay tesselation. Kochanek & Dalal (2003), however, used SIS clumps of a mass of $10^6 M_\odot$ and since these are more numerous, they can enhance the effect. Further, fitting SIE to the data is not fully justified, especially concerning the profile of our mass distribution. For observed lenses, the mass profile is known only for a handful of lenses. Whereas the lens galaxies in MG1654+134, MG2016+112, 0047–281, and B1933+503 have an isothermal profile, the one of PG1115+080 seems to be steeper (see Kochanek 1995; Cohn et al. 2001; Treu & Koopmans 2002a,b; Koopmans & Treu 2003). Besides the absence of substructure on scales $\lesssim 10^7 M_\odot$, our synthetic systems and their modelled quantities closely resemble the properties of realistic lenses and the way in which these are modelled.

In the analysis of Kochanek & Dalal (2003) the synthetic images were generated using an SIE macromodel with SIS substructure. This makes the fitting less difficult and explains why they get a transition of cumulative distribution at $\ln(\mu_{\text{obs}}/\mu_{\text{mod}}) \sim 0$, where μ_{obs} are the magnification factors taken directly from N-body simulations and μ_{mod} are the ones from best fit SIE+SH models.

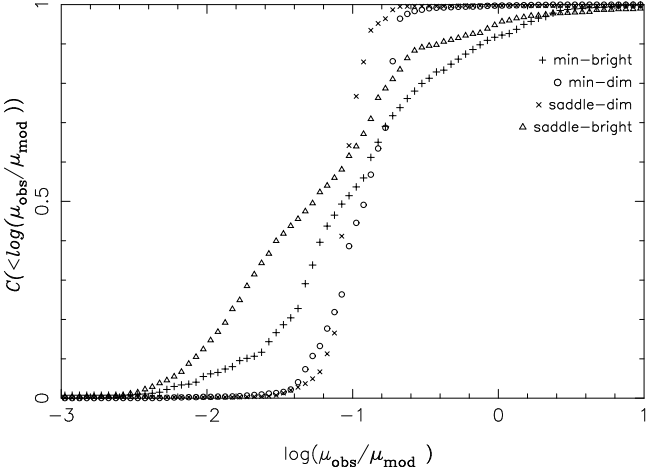


Fig. 7. The cumulative flux residuals for each type of image. Synthetic image systems were taken from the elliptical halo (see also Fig. 2a). Only image positions from the systems with $\mu_{\text{tot}} > 20$ generated from the elliptical halo were fitted using SIE+SH. μ_{obs} are the magnification factors taken directly from N-body simulations and μ_{mod} are the ones from best fit SIE+SH models

We are aware of the fact that the saddle point suppression can partly be an artifact of the noise in our simulation, especially since we know that even very low mass structures, when present in amount, can produce this effect. The effect is not present when smoothing κ on scales above $\sigma_G \sim 2$ kpc. However we also effectively smooth out together the noise and physical substructure.

We have looked at the cumulative flux mismatch distribution of one bootstrapped map to investigate the accuracy of the distribution. There is only a slight indication that the bright saddle point is demagnified w.r.t. the bright minimum in the bootstrapped map. One therefore has to take the results with caution and constantly keep in mind that they are affected by both physical substructure and noise.

5. Conclusion

In this work we have done a pilot study of the strong gravitational lensing behaviour of N-body simulated galaxies. We especially concentrated on the influence of substructure on flux ratios. Such an analysis is crucial in order to understand the lensing signal we observe from realistic lenses and to disentangle the influence on lensed-image fluxes coming from propagation effects in ISM and originating from substructure.

We have examined two strong lens signatures of substructure, i.e. the broken cusp relation observed in images that show a typical cusp configuration and the saddle point suppression. The saddle point suppression has been previously studied using a semi-analytic prescription of substructure (Schechter & Wambsganss 2002; Kochanek & Dalal 2003). The effect of substructure on

the cusp relation, however, has not been studied in detail previously.

In order to determine the magnitude of both effects we use N-body simulated galaxies. The difference compared to the works of Schechter & Wambsganss (2002) and Kochanek & Dalal (2003) is that we are using profiles of substructure which are as realistic as possible and do not make any assumptions on the mass function and abundance of sub-halos. The drawback, however, is the resolution of the simulations. We are therefore not able to extrapolate the analysis to masses $\lesssim 10^7 M_\odot$. Still, the signatures of both effects are seen and in future we plan to use higher-resolution N-body simulations to explore them in detail.

The main question when dealing with N-body simulation is how much are the magnification factors we use for synthetic image systems affected by noise which can mimic substructure of $\lesssim 10^7 M_\odot$. We have shown that the average relative noise in the surface mass density $\sigma(\kappa)/\kappa$ lies well below $\sim 5\%$ level for $\kappa \gtrsim 0.5$. Further results from the bootstrap analysis indicate that R_{cusp} is not dominantly affected by the noise, but by physical substructure; for saddle point suppression the conclusion is less clear at this point.

The behaviour of R_{cusp} for sources close to a cusp is in principle a very promising tool to detect substructure. Its main advantage is that it makes definite, model-independent predictions for magnifications and that the prediction can only be broken in the presence of substructure. In Fig. 2, where we used a simulated elliptical galaxy to calculate R_{cusp} , we can clearly see these effects of substructure. When smoothing out the substructure on larger scales we effectively observe the pattern that is common for generic SIE lens model.

However, the disc in the spiral galaxy can also help to destroy the cusp relation for sources in the vicinity of a cusp. We have calculated the cusp relation pattern for the simulated spiral galaxy, and even in the absence of obvious substructure in the form of clumps we can see strong violations of the cusp relation. This is expected, since the disc in edge on projection gives κ -variations on the scales smaller than the image separation and has to be viewed as substructure in the lens potential. One therefore cannot conclude from the broken cusp relation alone that we observe the signatures of substructure in the form of clumps. However, the observations show that most observed lenses are elliptical and therefore one can concentrate on this morphology only. Still, detailed modelling is required in most cases (e.g. B1422+231) to clearly see the effect.

The phenomenon of suppressed saddle point is a very strong prediction that could possibly rule out a significant influence of the ISM on flux anomalies. If the flux anomalies depend on parity and magnification they must clearly be caused by lensing itself. There is one exception, namely the less magnified images are more compact and they can be influenced more strongly by scatter broadening and scintillation. Again, this is in contrast with observations,

where flux perturbations seem to show parity dependence and are more obvious for highly magnified images.

Our analysis shows that the two brighter images are on average more affected by substructure than the two dimmer ones. In addition, there is an indication that the brightest saddle point image in N-body simulated systems has a higher probability to be demagnified, in accordance with predictions from microlensing and from semi-analytic work by (Kochanek & Dalal 2003).

For future work, we plan to look for jet curvature as seen from N-body simulations. At present, there is only one case of a curved jet observed that is likely the cause of gravitational lensing (Metcalfe 2002). It will be interesting, however, to investigate the probability of more of these occurrences. We are planning to investigate the signal one expects on average for multiple-imaged jets; this signal is also less affected by noise in the simulation and low-mass substructure.

In summary, gravitational lensing remains a very powerful tool for testing the existence of CDM substructure. Systematics on flux anomalies (scatter broadening, scintillation, microlensing) can be efficiently ruled out by multi-frequency and higher-frequency observations of lenses. Furthermore, the statistical analysis of lenses can directly show the effects of CDM substructure on lenses. In addition, N-body simulated galaxies do seem to produce the same effects as seen in observed lens systems.

Acknowledgements. We would like to thank Oleg Gnedin, Chris Kochanek and Oliver Czoske for many useful discussions that helped improve the paper, Vincent Eke for providing us with the simulation data and Richard Porcas for careful reading of the manuscript. This work was supported by the International Max Planck Research School for Radio and Infrared Astronomy at the University of Bonn, by the Bonn International Graduate School, by the Deutsche Forschungsgemeinschaft under the project SCHA 342/3-1, and by the NASA ATP program under grant NAG 5-10827.

References

- Abadi, M. G., Navarro, J. F., Steinmetz, M., & Eke, V. R. 2002a, astro-ph/0211331
- . 2002b, astro-ph/0212282
- Barber, B. C., Dobkin, D. P., & Huhdanpaa, H. 1996, ACM Transactions on Mathematical Software, 22, 469
- Barkana, R. 1998, ApJ, 502, 531
- Benson, A. J., Frenk, C. S., Lacey, C. G., Baugh, C. M., & Cole, S. 2002, MNRAS, 333, 177
- Blandford, R. & Narayan, R. 1986, ApJ, 310, 568
- Blandford, R. D. 1990, QJRAS, 31, 305
- Blandford, R. D. & Kochanek, C. S. 1987, ApJ, 321, 658
- Bode, P., Ostriker, J. P., & Turok, N. 2001, ApJ, 556, 93
- Bradač, M., Schneider, P., Steinmetz, M., et al. 2002, A&A, 388, 373
- Bullock, J. S., Kravtsov, A. V., & Weinberg, D. H. 2000, ApJ, 539, 517
- Chen, J., Kravtsov, A. V., & Keeton, C. R. 2003, astro-ph/0302005

- Chiba, M. 2002, *ApJ*, 565, 17
- Cohn, J. D., Kochanek, C. S., McLeod, B. A., & Keeton, C. R. 2001, *ApJ*, 554, 1216
- Colín, P., Avila-Reese, V., & Valenzuela, O. 2000, *ApJ*, 542, 622
- Dalal, N. & Kochanek, C. S. 2002, *ApJ*, 572, 25
- de Blok, W. J. G. & Bosma, A. 2002, *A&A*, 385, 816
- Evans, N. W. & Witt, H. J. 2002, *astro-ph/0212013*
- Frigo, M. & Johnson, S. 1998, in 1998 ICASSP conference proceedings, Vol. 3, 1381
- Gaudi, B. S. & Petters, A. O. 2002, *ApJ*, 574, 970
- Grogin, N. A. & Narayan, R. 1996, *ApJ*, 464, 92
- Hayashi, E., Navarro, J. F., Taylor, J. E., Stadel, J., & Quinn, T. 2003, *ApJ*, 584, 541
- Heyl, J. S., Hernquist, L., & Spergel, D. N. 1994, *ApJ*, 427, 165
- Keeton, C. 2001, *astro-ph/0112350*
- Keeton, C. R. 2003, *ApJ*, 584, 664
- Keeton, C. R., Gaudi, B. S., & Petters, A. O. 2002, *astro-ph/0210318*
- Klypin, A., Kravtsov, A. V., Valenzuela, O., & Prada, F. 1999, *ApJ*, 522, 82
- Kochanek, C. S. 1995, *ApJ*, 445, 559
- Kochanek, C. S. & Dalal, N. 2003, *astro-ph/0302036*
- Koopmans, L. & de Bruyn, A. 2000, *A&A*, 358, 793
- Koopmans, L. V. E., Biggs, A., Blandford, R. D., et al. 2003, *astro-ph/0302189*
- Koopmans, L. V. E. & Treu, T. 2003, *ApJ*, 583, 606
- Kormann, R., Schneider, P., & Bartelmann, M. 1994, *A&A*, 284, 285
- Kravtsov, A. V., Klypin, A. A., Bullock, J. S., & Primack, J. R. 1998, *ApJ*, 502, 48
- Lombardi, M. & Schneider, P. 2002, *A&A*, 392, 1153
- Mao, S. 1992, *ApJ*, 389, 63
- Mao, S. & Schneider, P. 1998, *MNRAS*, 295, 587
- Metcalf, R. 2002, *ApJ*, 580, 696
- Metcalf, R. B. & Madau, P. 2001, *ApJ*, 563, 9
- Metcalf, R. B. & Zhao, H. 2002, *ApJ*, 567, L5
- Meza, A., Navarro, J. F., Steinmetz, M., & Eke, V. R. 2003, *astro-ph/0301224*
- Moore, B. 1994, *Nature*, 370, 629
- Moore, B., Ghigna, S., Governato, F., et al. 1999, *ApJ*, 524, L19
- Navarro, J. & Steinmetz, M. 1997, *ApJ*, 478, 13
- Press, W. H., Teukolsky, S. A., Vetterling, W. T., & Flannery, B. P. 1992, *Numerical recipes in C. The art of scientific computing* (Cambridge: University Press, 1992, 2nd ed.)
- Quadri, R., Moeller, O., & Natarajan, P. 2002, *astro-ph/0212465*
- Schaap, W. E. & van de Weygaert, R. 2000, *A&A*, 363, L29
- Schechter, P. L. & Wambsganss, J. 2002, *ApJ*, 580, 685
- Schneider, P., Ehlers, J., & Falco, E. 1992, *Gravitational Lenses (Gravitational Lenses*, Springer-Verlag Berlin Heidelberg New York.)
- Schneider, P. & Weiss, A. 1992, *A&A*, 260, 1
- Somerville, R. S. 2002, *ApJ*, 572, L23
- Spergel, D. N. & Steinhardt, P. J. 2000, *Physical Review Letters*, 84, 3760
- Springel, V. & Hernquist, L. 2003, *MNRAS*, 339, 289
- Steinmetz, M. 1996, *MNRAS*, 278, 1005
- Steinmetz, M. & Navarro, J. 2000, in *ASP Conf. Ser.* 197: *Dynamics of Galaxies: from the Early Universe to the Present*, eds. F. Combes, G. A. Mamon, and V. Charmandaris., 165
- Steinmetz, M. & Navarro, J. F. 2003, *New Astronomy*, 8, 557
- Stoehr, F., White, S. D. M., Tormen, G., & Springel, V. 2002, *MNRAS*, 335, L84
- Swaters, R. A., Madore, B. F., & Trehewella, M. 2000, *ApJ*, 531, L107
- Treu, T. & Koopmans, L. V. E. 2002a, *ApJ*, 575, 87
- . 2002b, *MNRAS*, 337, L6
- van den Bosch, F. C. & Swaters, R. A. 2001, *MNRAS*, 325, 1017
- Witt, H. J., Mao, S., & Schechter, P. L. 1995, *ApJ*, 443, 18
- Woźniak, P. R., Udalski, A., Szymański, M., et al. 2000, *ApJ*, 540, L65
- Zentner, A. R. & Bullock, J. S. 2003, *astro-ph/0304292*